Published in final edited form as:

NMR Biomed. 2024 May ; 37(5): e5102. doi:10.1002/nbm.5102.

Transmembrane pH gradient imaging in rodent glioma models

Sandeep Kumar Mishra[1], **Jessica Gois Santana**[2], **Jelena Mihailovic**[1], **Fahmeed Hyder**[1,2], **Daniel Coman**[1,2]

[1]Yale University, Department of Radiology & Biomedical Imaging, New Haven, CT 06510, USA

[2]Yale University, Department of Biomedical Engineering, New Haven, CT 06510, USA

Abstract

A unique feature of the tumor microenvironment is extracellular acidosis in relation to intracellular milieu. Metabolic reprogramming in tumors results in overproduction of H^+ ions (and lactate), which are extruded from the cells to support tumor survival and progression. As a result, the transmembrane pH gradient (ΔpH), representing the difference between intracellular pH (pH_i) and extracellular pH (pH_e), is larger in tumors compared to normal tissue. Controlling the transmembrane pH difference holds promise as a potential therapeutic target in cancer and plays an important role in regulating drug delivery into cells. The present study shows successful development of an MR-based technique that provides ΔpH imaging at sub-millimeter resolution. We applied this technique to image ΔpH in rat brains with RG2 and U87 gliomas, as well as in mouse brains with GL261 gliomas. pH_i was measured with Amine and Amide Concentration-Independent Detection (AACID), while pH_e was measured with Biosensor Imaging of Redundant Deviation in Shifts (BIRDS). The results indicate that pH_i was slightly higher in tumors (7.40–7.43 in rats, 7.39–7.47 in mice) compared to normal brain (7.30–7.38 in rats, 7.32–7.36 in mice), while pH_e was significantly lower in tumors (6.62–6.76 in rats, 6.74–6.84 in mice) compared to normal tissue (7.17–7.22 in rats, 7.20–7.21 in mice). As a result, ΔpH was higher in tumors (0.64–0.81 in rats, 0.62–0.65 in mice) compared to normal brain (0.13–0.16 in rats, 0.13–0.16 in mice). This work establishes an MR-based platform for ΔpH imaging at sub-millimeter resolution in gliomas.

Graphical Abstract

Corresponding author: Daniel Coman, Ph.D., 300 Cedar St, TAC N136, New Haven, CT 06520, USA; daniel.coman@yale.edu.

CONFLICT OF INTEREST STATEMENT

Fahmeed Hyder is the founder of Innovacyclics LLC. All other authors declare no conflicts of interest.

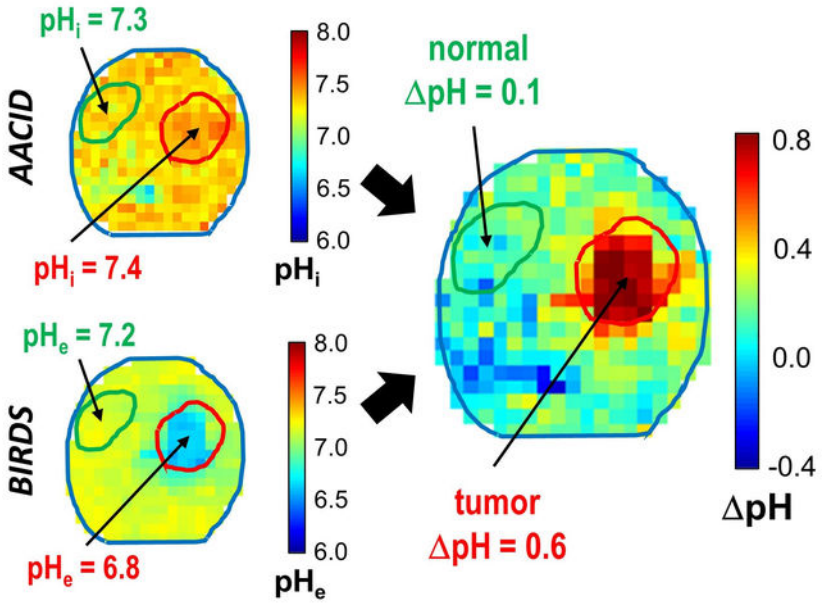

We demonstrate feasibility of imaging the transmembrane pH gradient (ΔpH) with MRI/MRSI at sub-millimeter resolution in both rat and mouse brains with various glioma models. The ΔpH was obtained by imaging intracellular pH with AACID and extracellular pH with BIRDS. This method can be used to investigate resistance mechanisms in cancer, regulation of drugs entry into cells or the effect of therapies that target ΔpH, leading to improved and personalized cancer treatments.

Keywords

MRS; MRI; transmembrane pH; intracellular pH; extracellular pH; AACID; BIRDS; glioma

INTRODUCTION

For uncontrolled proliferation, cancer cells require elevated glucose metabolism thereby suppressing oxidative metabolism in mitochondria compared to normal cells, even when enough oxygen is available. This dysbolism phenomenon is referred to as “aerobic glycolysis” or the “Warburg effect” [1–4], and results in excessive production of hydrogen (H^+) ions and lactate, which are subsequently extruded from the cells to maintain an alkaline intracellular pH (pH_i) environment essential for sustaining the function of intracellular machinery (i.e. glycolytic enzymes) [5, 6]. Therefore, the extracellular pH (pH_e) in the tumor microenvironment is lower in relation to intracellular milieu, and the transmembrane pH gradient ($\Delta pH=pH_i-pH_e$) is much larger in tumors compared to normal tissue [7–10], which results in a reversed pH gradient in tumors, observed originally by Stubbs et al. [11, 12]. This extracellular acidosis activates matrix metalloproteases and cathepsins promoting tumor growth and metastasis [13], supports tumor survival and progression [4] and resistance to therapy [3]. However, the large ΔpH specific to tumor cells could provide an excellent target for treatment of cancer [14–16], while regulating the acidic pH_e and neutral/alkaline pH_i can be exploited by weak acid chemotherapeutics to specifically increase drug uptake by cancer cells [17–21]. Thus, imaging ΔpH could be very beneficial

for better understanding cancer progression, resistance to existing treatments and designing improved therapies.

Currently, the availability of techniques for *in vivo* ΔpH imaging is quite limited, especially in clinical settings. Non-invasive pH imaging can be achieved using magnetic resonance imaging (MRI) or spectroscopic imaging (MRSI). Specifically, ^{31}P MRSI of phosphate and phosphocreatine enables pH_i imaging [22], while ^{31}P MRSI of nontoxic exogenous agents like 3-aminopropyl phosphonate allows pH_e imaging [23]. However, due to long relaxation times (seconds) of ^{31}P signals, the resulting maps exhibit low spatial (e.g. 1.6mm×1.6mm×1.6mm) and/or temporal (several hours) resolutions [24]. An alternative approach is ^{19}F MRSI, which allows pH_e measurements [25, 26] and offers better sensitivity and dynamic range of pH-dependent ^{19}F frequencies compared to ^{31}P MRSI [27]. Nonetheless, ^{19}F MRSI also suffers from limitations such as coarse spatiotemporal resolution and lack of heteronuclear ^{19}F detector coils, particularly in clinical settings. Positron emission tomography (PET) is suitable for measuring specific targets in glioblastoma [28], but also faces challenges such as coarse spatial resolution (e.g. 1.4mm×1.4mm×1.4mm) and the inability to simultaneously and individually probe the intracellular and extracellular environments. Recently, there have been developments of dual MR/PET agents for pH imaging, but their pH sensitivity is somewhat reduced since the method relies on measuring both agent's concentration (using PET) and water longitudinal relaxation time T_1 (using MRI)[29, 30].

Chemical Exchange Saturation Transfer (CEST) is an MRI-based method that uses the proton exchange between the bulk water and exchangeable groups like amide, amine, or hydroxyl to image pH [31, 32]. A ratiometric approach, in which the ratio between the CEST signals from two different exchangeable groups is calculated, is commonly used for quantitative pH measurements, ensuring independence from water relaxation rates or concentration of exchange sites [31]. However, the pH quantification may be affected by other confounding factors such as unknown temperature, multiple exchangeable pools, magnetization transfer effects, or B_0 and/or B_1 field inhomogeneities [33]. pH_i imaging at high resolution can be obtained using a ratiometric CEST method called Amine and Amide Concentration-Independent Detection (AACID). This method utilizes a ratio calculated form the amine and amide CEST signals (which are predominantly from intracellular molecules) and is insensitive to small temperature variations [34]. The accuracy of AACID can be improved by applying a B_0 field correction using WAter Saturation Shift Referencing (WASSR), which takes into account the inhomogeneities of the magnetic field B_0 [35]. pH_e imaging of tumor and normal tissue at high resolution can also be obtained both preclinically and clinically with acidoCEST, a CEST technique based on a ratiometric approach using two amide proton signals from clinically approved CT contrast agents like iopamidol [36–38] or iopromide [39].

To obtain pH_e imaging at high resolution (e.g. 1mm isotropic or higher) we previously developed a ^{1}H MRSI method called Biosensor Imaging of Redundant Deviations in Shifts (BIRDS). This innovative approach combines high spatial resolution of MRI with high molecular specificity of MRS into a 3D MRSI platform [40–43]. BIRDS detects ^{1}H signals from lanthanide (Ln^{3+})-based macrocyclic agents like $TmDOTP^{5-}$, which

is a coordinate complex of paramagnetic thulium (Tm^{3+}) ion and macrocyclic chelate DOTP (1,4,7,10-tetraazacyclododecane-1,4,7,10-tetrakis(methylenephosphonate)) [40, 41]. In general, BIRDS uses non-exchangeable ^{1}H signals which are significantly shifted by the presence of the of paramagnetic Tm^{3+} ion, although in some cases signals from exchangeable groups like amides (-NH) can be also used. BIRDS signals possess extremely short relaxation times (0.1–10 ms), enabling ultra-fast acquisitions and are sensitive reporters of environment parameters like pH or temperature [40]. Since exogenous agents like $TmDOTP^{5-}$ could not access the intracellular space, BIRDS measurements reflect exclusively the extracellular compartment (i.e., pH_e). BIRDS with $TmDOTP^{5-}$ has been used on 9.4T and 11.7T preclinical scanners for pH_e imaging of murine brain tumors [22, 44–47], and of rabbit liver tumors on clinical 3T scanners [48–52]. In the current work we developed a novel high resolution ΔpH imaging method by combining pH_i imaging (with AACID) and pH_e imaging (with BIRDS) and we applied this technique in rat brains with orthotopic RG2 and U87 gliomas, and in mice brains with GL261 gliomas. We evaluated this novel technique on brain glioma models due to their suitability as a tumor model for extremely aggressive, highly glycolytic, and strongly pH-dependent brain malignancies. Gliomas exhibit poor prognosis, high resistance to chemotherapy, and short survival periods almost unchanged in the past four decades [6, 53–56].

MATERIALS AND METHODS

Glioma animal models

We used three different glioma models, RG2, U87 and GL261 to evaluate the feasibility of the transmembrane pH gradient imaging method proposed. The malignant RG2 model is a rat-derived glioma model that develops in Fisher 344 rats [57], U87 is a human-derived glioma model that grows in athymic/nude rats [58], while GL261 is a murine glioma model created by chemical induction with methylcholanthrene that grows in C57BL/6 mice [59]. RG2 and U87 cells were procured from the American Type Culture Collections. The GL261 cells were kindly provided by DeFeyter's group at Yale University. All three cell types were cultured in 75 cm^3 culture flasks in an incubator with 5% CO_2 atmosphere at 37°C. The culture medium used was the high-glucose (4.5 g/L) Dulbecco's modified eagle's medium (DMEM) supplemented with 10% heat-inactivated fetal bovine serum and 1% penicillin-streptomycin. Only cells at a low passage number (<20) were utilized. Prior to intracranial injection, the cells were harvested when they reached a high confluence (>80%) and suspended in serum-free DMEM.

All animal protocols were approved by the Institutional Animal Care and Use Committee at Yale University. Fisher 344 rats (220–300 g, females), athymic/nude rats (150–250 g, females) and C57BL/6J mice (25–30 g, males; Charles River Laboratories, Boston, MA) were housed and maintained in specific pathogen-free conditions for a minimum of two weeks prior to intracranial tumor implantation. To perform intracranial cell injections, the animals were anesthetized with isoflurane (2–3%). The animals were secured in a stereotactic holder and their scalp was sterilized with betadine and 70% ethanol. Prior to making a midline incision in the scalp, local anesthetic (bupivacaine, 2 mg/kg) was administered. After exposing the skull, a hole was drilled with a motorized drill, positioned

3 mm for rats and 2 mm for mice to the right of the bregma. To perform the intercranial injection, a 5 μL suspension containing either 2.5×10^3 RG2 cells, 2×10^5 U87 cells or 1×10^5 GL261 cells was loaded into a 10-μL Hamilton syringe equipped with a 26G needle. The burr hole was used as a point of entry for the needle, which was then carefully positioned and inserted 3 mm for rats and 2 mm for mice below the dura into the right striatum. The cells were administered using a microinfusing pump at a rate of 1 μL/min over a period of 5 minutes. After the injection, the needle was left in place for 5 minutes to minimize the risk of cell backflow from the injection site. Subsequently, to ensure that no cells escaped from the injection site, the needle was slowly withdrawn at a rate of 0.5 mm/min. Bone wax was applied to seal the burr hole, and the incision site was sutured and sterilized. For pain management, carprofen (5 mg/kg) was administered subcutaneously during the procedure, and this treatment continued for 48 hours after the surgery to provide analgesia. The animals were closely monitored daily for any signs of weight loss or development of neurological symptoms. Tumor growth was monitored starting at day 10 after implantation of tumor cells.

MRI and MRSI data acquisition in rats

The MRI and MRSI data were obtained on a 9.4T Bruker horizontal bore spectrometer (Billerica, MA, USA) using a volume transmit/surface receive ^{1}H radio frequency (RF) dual coil. The volume RF coil had an inner diameter of 50mm. The surface RF coil had a saddle shape with a length of 25mm and width of 20mm. $TmDOTP^{5-}$ was purchased from Macrocyclics (Dallas, TX, USA). Probenecid, an organic anion transporter inhibitor which can slow renal clearance of contrast agents, was used to temporarily increase the $TmDOTP^{5-}$ concentration [46, 60]. Co-infusion of $TmDOTP^{5-}$ with probenecid was necessary because a lower $TmDOTP^{5-}$ concentration (less optimal for BIRDS detection) was measured previously in most organs, indicating a faster clearance rate in the absence of probenecid treatment [46]. Probenecid was originally designed to decrease the renal excretion of antibiotics and is currently used in patients for gout treatment due to its uricosuric characteristics [61]. Although there is evidence that probenecid inhibits organic cation transport in kidneys [62], there is no evidence that this drug causes a perturbation of proton transport or affects the transmembrane pH gradient in the brain. The animals were placed on a heating pad to maintain body temperature, artificially ventilated (70% N_2O/30% O_2) and anesthetized with 3% isoflurane. A PE10 (Braintree Scientific, LLC) tail vein line was inserted for probenecid and $TmDOTP^{5-}$ infusion. Heparinized saline (~30–50 μL) was flushed through the line every 30 min throughout the imaging session to prevent clotting. Paralube ointment was applied to the eyes to prevent dryness. The animals were positioned in a prone orientation in a 3D printed plastic holder and inserted in the dual RF coil. During MR data acquisition, the animals were artificially ventilated (70% N_2O / 30% O_2) and kept under anesthesia (1–2% isoflurane). The breathing rate was monitored using a respiratory monitor, while the body temperature was maintained using a circulating warm water heating pad and monitored using a rectal fiber-optic temperature probe.

The MRI datasets were obtained using the volume RF coil for transmission and the surface RF coil for acquisition. T_1-weighted images were obtained using a field-of-view (FOV) of 32mm×32mm, 128×128 matrix size, 9 slices of 1mm thickness, repetition time (TR) = 1.5s and echo time (TE) = 10ms. Both WASSR and AACID were obtained using a

spin-echo-based echo-planar imaging (EPI) sequence with an FOV of 32mm×32mm, 1 slice of 1mm thickness, a TR of 6s for WASSR and 8s for AACID, a TE of 20ms and an image matrix of 42×42, for an in-plane voxel resolution of 0.76mm×0.76mm. For WASSR, a 4s continuous wave of 0.2μT was used for saturation of 61 offset frequencies in the range from −500 to 500 Hz. For AACID, a 4s continuous wave of 1.5μT was used for saturation of 70 offset frequencies in the range from −8000 to 8000 Hz, non-equally distributed and specifically chosen to define more accurately the amide (3.5ppm) and amine (2.75ppm) peaks. The total acquisition time was 6 minutes for WASSR and 19 minutes for AACID.

After acquisition of all MRI datasets, 100 mg/kg probenecid was administered over 10 min, followed by a waiting period of 20 min and then by co-infusion of 100 mg/kg probenecid and 1 mmol/kg $TmDOTP^{5-}$. All infusions were performed using a syringe pump at a rate of 15 μL/min for a total infusion time of 90 min. BIRDS technique using MRSI was extensively described previously [22, 40, 41, 43, 50, 63, 64]. BIRDS datasets were acquired using the surface RF coil for both transmission and acquisition. Selective excitation of H2, H3 and H6 protons of $TmDOTP^{5-}$ was achieved using a dual-band 340μs Shinnar-Le Roux (SLR) RF pulse. Water-suppression was not necessary because the dual-band SLR pulse produces minimal excitation of the water signal [50]. The 3D MRSI datasets for BIRDS were obtained using a TR of 6ms, a spectral window of 200kHz, 1024 points, an FOV of 25mm×25mm×29mm, 160 averages, 1199 spherical encoding steps, and 19 minutes total acquisition time. BIRDS datasets were reconstructed to a 25×25×29 matrix for a $1mm^3$ isotropic voxel resolution. For BIRDS we preferred a 3D MRSI sequence to a more commonly used 2D sequence because the chemical shifts of $TmDOTP^{5-}$ protons are spread over more than 200ppm, which would result in a significant and non-identical spatial displacement of these MR signals during the slice selection gradient in a 2D MRSI acquisition. However, no spatial displacement is expected for AACID (obtained using a 2D EPI-MRI sequence) because the acquisition is based on a single “on-resonance” water signal.

MRI and MRSI data acquisition in mice

Animal preparation and data acquisition in mice closely resembled those in rats. Below, we provide only the details that differ from the experiments conducted in rats. The T_1-weighted images were obtained using an FOV of 25mm×25mm and 15 slices of 0.5mm thickness. The WASSR and AACID were obtained using an EPI sequence with an FOV of 25mm×25mm, for an in-plane voxel resolution of 0.6mm×0.6mm. Both probenecid and $TmDOTP^{5-}$ were delivered intraperitonially. Initially, a probenecid bolus (100 mg/kg) was administered, followed by a waiting period of 20 minutes. After this, co-infusion of probenecid and $TmDOTP^{5-}$ was done for 90 minutes at 120–140 μL/hour. BIRDS datasets were obtained using an FOV of 19mm×15mm×25mm, 256 averages, 623 spherical encoding steps, and 16 minutes total acquisition time. BIRDS datasets were reconstructed to a 19×15×25 matrix for a $1mm^3$ isotropic voxel resolution.

MRI and MRSI data processing

All MR data processing was done in MATLAB (MathWorks Inc., Natick, MA). The “B_0 correction” required for AACID data processing was done using WASSR [35]. The signal

from each voxel in the series of WASSR images (Fig. 1A) was plotted to obtain the WASSR Z-spectrum for that voxel (Fig. 1B). The water peak in each Z-spectrum was then fitted with a Lorentzian function using a least-squares approach (Fig. 1B). The B_0 shift of water signal (in Hz, Fig. 1B) was calculated as the frequency difference (or offset) between the top of the Lorentzian fit and the spectrometer frequency (for which a zero offset was assigned). The B_0 map (Fig. 1C) was generated using the B_0 shifts from each voxel. Next, for AACID data processing, the series of AACID images (Fig. 1D) were used to generate a Z-spectrum in each voxel (Fig. 1E). An accurate estimation of amine and amide CEST signals requires measurement of signals at their exact frequency offsets (1102Hz for amine and 1402Hz for amide, relative to water signal). However, the frequency of the water signal (which is proportional to the B_0 field) was different in each voxel (Fig. 1C), and thus the alignment of all Z-spectra from all voxels was required, with the water signal set to zero offset. This procedure is called "B_0 correction" (Fig. 1E–F) and was achieved by first creating a higher resolution Z-spectrum by spline interpolation (with datapoints at every 1Hz), followed by shifting of the entire Z-spectrum along the frequency axis by an amount equal to the B_0 shift (measured by WASSR). This procedure ensured the proper alignment of amine and amide CEST signals in each voxel. The spline interpolation step employed to increase the resolution of the Z-spectrum is a very commonly used procedure for CEST data processing and was necessary because sampling of CEST data at 1Hz resolution would result in extremely long experiment durations (several hours) which was not feasible. The AACID ratio was calculated from the "B_0 corrected" CEST signals from amine ($S_{2.75ppm}$), amide ($S_{3.50ppm}$), and a reference signal ($S_{6.00ppm}$) according to [34]:

$$AACID = \frac{\frac{S_{6.00ppm}}{S_{2.75ppm}} - 1}{\frac{S_{6.00ppm}}{S_{3.50ppm}} - 1} \quad (1)$$

The pH_i was calculated from the AACID ratio assuming a linear dependence according to:

$$pH_i = m \bullet AACID + c \quad (2)$$

where m = −1.42 and c = 11.61 [65].

The pH_e was calculated in each MRSI voxel from the ^1H chemical shifts δ_2, δ_3 and δ_6 of H2, H3 and H6 protons of $TmDOTP^{5-}$, respectively, as previously described [40, 41, 50]. Briefly, a multi-parametric second order polynomial equation was used to describe the relationship between pH_e and $TmDOTP^{5-}$ chemical shifts:

$$pH_e = a_0 + \sum_{k=2,3,6} a_1^k \delta_k + \sum_{k=2,3,6} \sum_{j=2,3,6} a_2^{kj} \delta_k \delta_j \quad (3)$$

where the parameters a_0, a_1^k and a_2^{kj} (k=2,3,6; j=2,3,6) were obtained from the non-linear least-squares fit of pH as a function of H2, H3 and H6 chemical shifts [40]. The native pH_e map was resampled to match the resolution of the pH_i map using a Gaussian weighting factor g_{nr} which depends on the 3-dimensional distance d_{nr} between the voxel n in the native pH_e map and the voxel r in the resampled pH_e map as:

$$g_{nr} = exp\left(-\frac{d_{nr}^2}{2b^2}\right) \quad (4)$$

where the width at half maximum is $w = 2\sqrt{2ln2}\, b$. The pH_e value in each voxel r of the resampled pH_e map, $pH_{e,r}$, was calculated as a spatially weighted contribution of all non-zero pH_e values from the native pH_e map, $pH_{e,n}$ using the Gaussian weighting factor g_{nr}:

$$pH_{e,r} = \frac{\sum_{n=1}^{N} g_{nr}\, pH_{e,n}}{\sum_{n=1}^{N} g_{nr}} \quad (5)$$

where N represents the number of voxels with non-zero pH_e in the native pH_e map.

Statistical analysis

All results were expressed in terms of mean ± standard deviation and all comparisons were assessed by Student's t test with two tails, where p-values of less than 0.05 were considered statistically significant.

RESULTS

Transmembrane pH imaging in rat brains with gliomas

Transmembrane pH gradient imaging requires acquisition of pH_i and pH_e maps. We used AACID for pH_i mapping [34] and BIRDS for pH_e mapping [22] in rats (n=4) with either RG2 or U87 tumors. Fig. 1 shows an example of ΔpH imaging in a rat brain with an RG2 tumor. WASSR was used for B_0 mapping [35], which was required for B_0 correction of AACID data. For WASSR, a series of 61 EPI-based MR images (Fig. 1A) were used to generate a Z-spectrum in each voxel (Fig. 1B). The Z-spectrum was fitted to a Lorentzian function (red line in Fig. 1B). The center of the Lorentzian fit represents the frequency offset of the water signal, and thus provides a measure of the B_0 field shift in that voxel (Fig. 1B) which can be used to generate the B_0 map (Fig. 1C). For AACID, a series of 70 EPI-based MR images (Fig. 1D) were used to generate a Z-spectrum in each voxel (Fig. 1E). A "B_0 corrected" Z-spectrum (red line in Fig. 1E and 1F) was obtained by spline interpolation at 1Hz resolution followed by a B_0 shift along the frequency axis using the B_0 map obtained with WASSR. The "B_0 corrected" Z-spectrum was used to measure the amide signal at 3.5ppm (green dashed line in Fig. 1F) and amine signal at 2.75ppm (orange dashed line in Fig. 1F). The amide and amine intensity maps are shown in Fig. 1G. The AACID

ratio (Fig. 1H) was calculated from the amine and amide signals, using as reference the signal at 6.0ppm (blue dashed line in Fig. 1E) according to eq.1 [34]. The pH_i (Fig. 1I) was calculated from the linear dependence between pH_i and AACID ratio according to eq.2 [34, 65]. A T_1-weighted MR image (Fig. 1J) was used to localize and define a region of interest (ROI) for the tumor (indicated with a black contour in Fig. 1) and delineate the entire brain (indicated with a blue contour in Fig. 1). A second ROI corresponding to normal brain tissue (indicated with a green contour in Fig. 1) was defined in the contralateral brain hemisphere for comparisons with tumor measurements. The average pH_i values measured in the tumor and normal tissue ROIs were 7.40 ± 0.07 and 7.31 ± 0.07, respectively (Fig. 1I).

For pH_e measurements with BIRDS, a fast 3D MRSI sequence (TR=6ms) at 1mm isotropic resolution was used (see Methods). The chemical shifts of H2, H3 and H6 protons from $TmDOTP^{5-}$ (shown in red, overlayed on the anatomical image in Fig. 1J) were used to calculate the pH_e in each voxel according to eq.3 [40]. The transmembrane pH gradient ΔpH is defined as the difference between the pH_i and pH_e in each voxel, $\Delta pH=pH_i-pH_e$. Thus, a resampling of the native pH_e map at 1mm isotropic resolution (Fig. 1K) to match the higher resolution of the pH_i map (0.76mm×0.76mm×1.00mm) is required. This was achieved by calculating the pH_e value in each voxel of the resampled map as a spatially weighted contribution of all non-zero voxels from the native pH_e map. For this, we used a Gaussian weighting factor g_{nr} which depends on the distance d_{nr} between voxel n from the native pH_e map and voxel r from the resampled pH_e map according to eq.4 with b=0.3mm, corresponding to a width at half maximum of 0.7mm (Fig. 1L). The pH_e values in the resampled pH_e map (Fig. 1M) were calculated according to eq.5. The resampled pH_e map shows similar features as the native pH_e map. The average pH_e values measured using the resampled pH_e map in the tumor and normal tissue ROIs were 6.76 ± 0.17 and 7.18 ± 0.04, respectively (Fig. 1M). The pH_i map (Fig. 1I) and pH_e map (Fig. 1M) were used to calculate the transmembrane pH gradient ΔpH map (Fig. 1N). The average ΔpH values in the RG2 tumor and normal tissue ROIs were 0.64 ± 0.18 and 0.13 ± 0.09, respectively (Fig. 1N).

Additional examples of ΔpH imaging in rat brains with RG2 and U87 tumors are shown in Fig. 2 and Supplementary Fig.1. Localization of tumors was based on T_1-weighted MR images (indicated with a black contour) and a second ROI (indicated with a green contour) was defined in the normal brain tissue from the contralateral hemisphere (Fig. 2Ai and 2Bi). The pH_i maps obtained with AACID indicate average values of 7.43 ± 0.06 and 7.36 ± 0.07 inside the RG2 tumor and in the normal tissue ROIs, respectively (Fig. 2Aii), while for the rat with U87 tumors, the average pH_i values were 7.43 ± 0.10 and 7.38 ± 0.05 in the tumor and normal tissue ROIs, respectively (Fig. 2Bii). The pH_e maps obtained with BIRDS and resampled to match the pH_i resolution show average pH_e values of 6.76 ± 0.09 and 7.21 ± 0.05 inside the RG2 tumor and in the normal tissue, respectively (Fig. 2Aiii). The average pH_e values inside the U87 tumor and in the normal brain tissue were 6.73 ± 0.09 and 7.22 ± 0.03, respectively (Fig. 2Biii). The ΔpH maps obtained from the pH_i and pH_e maps indicate average ΔpH values of 0.67 ± 0.14 and 0.15 ± 0.08 inside and outside the RG2 tumor, respectively (Fig. 2Aiv), while for the rat with U87 tumor the average ΔpH values were 0.70 ± 0.13 and 0.16 ± 0.05 inside and outside the tumor, respectively (Fig. 2Biv). For visual comparison, the average pH_i, pH_e and ΔpH values for all four rats investigated are shown as histograms in Fig. 2C–2E. Statistical analysis using Student's t-test with two tails indicate

that in three out of four rats the average pH_i was significantly higher ($p < 0.005$, Fig. 2C) in the tumor ROI compared to normal brain tissue. A similar analysis indicates that the pH_e values were significantly lower inside tumors ($p < 10^{-12}$, Fig. 2D), while ΔpH values were significantly higher inside tumors ($p < 10^{-12}$, Fig. 2E), when compared to normal tissue, in all rats investigated. The numerical pH_i, pH_e and ΔpH average values for all rats are given in Table 1. Histograms showing the distribution of pH_i, pH_e and ΔpH values for each individual ROI in all rats are given in Supplementary Fig. 2.

Transmembrane pH imaging in mouse brains with gliomas

Transmembrane pH gradient imaging was also obtained in mice with GL261 tumors (Fig. 3). The T_1-weighted MR images were used to localize and define the ROIs for the tumor and normal brain tissue (Fig. 3Ai). The pH_i maps were obtained with AACID (Fig. 3Aii). The pH_e maps were obtained with BIRDS and resampled to match the pH_i resolution (Fig. 3Aiii). The ΔpH maps were calculated from the difference between the pH_i and pH_e maps (Fig. 3Aiv). The results indicate average pH_i values of 7.39 ± 0.06 and 7.36 ± 0.05, average pH_e values of 6.77 ± 0.09 and 7.20 ± 0.03, and average ΔpH values of 0.62 ± 0.13 and 0.16 ± 0.04 in the tumor and normal tissue ROIs, respectively. Student's t-test analysis indicate that in two out of three mice the average pH_i was significantly higher ($p < 0.003$, Fig. 3B) in the tumor ROI compared to normal brain tissue. For all mice the average pH_e was significantly lower inside tumors ($p < 10^{-14}$, Fig. 3C) and the average ΔpH significantly higher inside tumors ($p < 10^{-14}$, Fig. 3D) when compared to normal tissue. Additional examples of pH_i, pH_e and ΔpH imaging in mouse brains are shown in Supplementary Fig.1. The numerical pH_i, pH_e and ΔpH average values for all mice are given in Table 1. The distribution of pH_i, pH_e and ΔpH values for each individual ROI in all mice are shown in Supplementary Fig. 3.

DISCUSSION

High resolution ΔpH imaging was achieved by combining pH_i and pH_e mapping in both rat and mouse brains with gliomas. pH_i imaging was obtained with AACID, an MR imaging sequence based on EPI that provided mapping at sub-millimeter resolution (0.76mm×0.76mm×1.00mm in rats, 0.6mm×0.6mm×1.00mm in mice). AACID is insensitive to changes in T_1 relaxation time, temperature, or reporter molecules concentration [34]. pH_e imaging with BIRDS in rat brains is a well-established technique in our lab [22, 45, 46, 66]. BIRDS is based on an ultrafast MRSI sequence which provides pH_e maps at 1mm isotropic resolution and is also independent on agent concentration or relaxation times. Although the same H2, H3 and H6 proton signals from $TmDOTP^{5-}$ can be used for both pH_e and temperature measurements, the use of multiple ^1H signals with different sensitivities allows determination of temperature and pH independently [40, 41]. Measurement of pH_i with AACID was calibrated and validated *in vivo* previously using ^{31}P MRS [34]. Validation of pH_e with BIRDS was done previously in 3D cell cultures also using two different ^{31}P MRS-based methods [64]. In the future, additional validation of pH_e may be obtained using the exogenous agent 3-aminopropylphosphonate [23].

In this study we report for the first time pH_e imaging with BIRDS in mouse brains (Fig. 3Aiii). To obtain pH_e maps with BIRDS in mice we followed a similar approach as in rat experiments. This included using probenecid to temporarily slowdown the renal clearance of the contrast agent and the use of an ultrafast MRSI sequence. The only difference was the *intraperitoneal* bolus administration of the contrast agent $TmDOTP^{5-}$. In both rats and mice, a 20-minute waiting period is necessary after initial probenecid dose for minimizing the $TmDOTP^{5-}$ clearance, while BIRDS signals become detectable after 30 minutes of $TmDOTP^{5-}$ infusion. Thus, including the durations required for probenecid/$TmDOTP^{5-}$ infusions, the total time required to obtain a pH_e image is 70 minutes, while a complete ΔpH image (including pH_i) requires 1.5 hours.

To upscale (increase) the resolution of pH_e imaging with BIRDS to match the resolution of pH_i imaging with AACID we implemented a simple resampling technique based on calculating the pH_e in every voxel of the resampled map as a spatially weighted contribution of every voxel from the native pH_e map, according to eq. 5. The spatially weighted contribution (Fig. 1L) was defined using a Gaussian function g_{nr} which depends on the distance d_{nr} between voxel n from the native map and voxel r from the resampled map according to eq.4. We tested several resampling approaches including the nearest neighbor, bicubic, bilinear, and the gaussian weighted approached employed in the current work. The nearest neighbor, bicubic and bilinear approaches all resulted in loss of information and/or incorrect calculation of pH_e values for the voxels at the edge of the brain, because some of their neighboring voxels have pH_e=0. However, when applying a gaussian weighted resampling approach, the voxels with pH_e=0 values do not contribute to the resampled image, according to eq.5. Moreover, a 3D gaussian weighted resampling is more accurate because it also takes into account the *distance* to the contributing voxel, such that farther voxels have smaller contributions. By using a small b value (b=0.3mm) we restricted the contribution to the resampled pH_e values only from nearest-neighbor voxels. To better illustrate this, using eq. 4 we calculated that a voxel positioned at a distance d_{nr}=1mm contributes only by 0.4% of the maximum possible contribution (100% at d_{nr}=0mm, when the two voxel positions coincide). A visual comparison between the native (Fig. 1K) and the resampled (Fig. 1M) pH_e maps indicate similar features, suggesting that the resampling approach preserves local characteristic variations in the pH_e values, both inside and outside tumor regions.

Extracellular acidosis is a distinct characteristic of cancer cells. The overproduction of H^+ ions and lactate arises as a consequence of increased glycolysis in cancer cells (even when oxygen is abundant) and suppressed oxidative phosphorylation in fully functional mitochondria, enabling them to evade apoptosis (Warburg effect) [1, 3, 4]. The efficient functioning of intracellular machinery essential for glycolysis (i.e. of enzymes involved in glycolysis) requires a slightly alkaline pH_i. To maintain an alkaline pH_i cancer cells employ various types of proton transporters like ion exchangers (e.g., Na^+-H^+ exchangers and vacuolar H^+-ATPase) and monocarboxylic acid transporters (MCTs) to extrude the H^+ ions into the extracellular space [5, 6]. Thus, we expect to observe an increased pH_i and a decreased pH_e in tumors, with the most aggressive and metastatic phenotypes having either a neutral or alkaline pH_i [1, 3], and a pH_e in the range of 6.2 to 7.0 [20, 67, 68]. Based on these observations, we hypothesize that the transmembrane pH gradient will be

significantly larger in tumors compared to normal tissue [7–10]. Our measurements indicate that the average pH_i values in both rat and mouse brains were slightly higher in tumors compared to normal brain tissue ($p<0.005$ in rats, Fig. 2C; $p<0.003$ in mice, Fig. 3B; Table 1). However, in one rat and one mouse this pH_i difference did not reached significance ($p>0.1$). The average pH_e values were significantly lower in all RG2 and U87 tumors in rats ($p<10^{-12}$, Fig. 2D) and in all GL261 tumors in mice ($p<10^{-14}$, Fig. 3C) compared to normal brain. In rats, the intratumoral-peritumoral pH_i and pH_e gradients (defined as the difference between the pH_i/pH_e values inside and outside the tumors) were $+0.09 \pm 0.03$ and -0.48 ± 0.06, respectively, while in mice these intratumoral-peritumoral pH_i and pH_e gradients were $+0.08 \pm 0.05$ and -0.42 ± 0.05, respectively. The intratumoral-peritumoral ΔpH gradients were $+0.57 \pm 0.08$ in rats and $+0.50 \pm 0.08$ in mice. Based on these results we conclude that the main contribution to significantly higher ΔpH values measured in tumors compared to normal brain in all rats ($p < 10^{-12}$, Fig. 2E) and mice ($p < 10^{-14}$, Fig. 3D) was the lower pH_e characteristic to tumor microenvironment, while pH_i had a much smaller contribution (<0.14, Table 1). Our pH_i measurements are consistent with previous longitudinal measurements in rat brains with C6 gliomas where the tumor pH_i (measured also using AACID) was significantly more alkaline ($p = 0.001$) compared to contralateral brain at all days [69]. However, their pH_e measurements using hyperpolarized ^{13}C bicarbonate MRSI indicate pH_e values higher than 7.0 in tumors [69]. This could be due to buffering properties of bicarbonate which could potentially affect the tumor pH_e as suggested by previous studies in rabbits [49, 52]. In addition, differences between tumor models could also account for these tumor pH_e differences.

Although the range of average tumor pH_i values measured in this work was relatively small (7.39–7.47), these average values were slightly higher than those of normal brain tissue (7.30–7.38) in all animals investigated (Table 1). As mentioned above, a slightly alkaline pH_i is necessary for efficient functioning of glycolysis machinery. Physiological changes in pH_i and/or pH_e can specifically regulate selected intracellular and extracellular proteins [70]. A pH_i increase represents a signal for cell proliferation [71–74], and promotes cell survival by limiting apoptosis (which is triggered by intracellular acidification) [75, 76], providing the advantages of growth-factor independent proliferation and evasion of apoptosis, two characteristics of most cancers [3, 77]. Therefore, measurement of both pH_i and pH_e is essential to monitor tumor progression and help identify potential therapeutic targets, such as physiological pH sensors or H^+ transporters.

Propagation of errors was used to estimate the error in ΔpH from the errors in signal measurements for both AACID and BIRDS. For AACID, assuming an error of 5% in the signal measurement, we estimate an error of 0.10 in the AACID ratio and an error of 0.14 in the pH_i measurement. For BIRDS, an SNR greater than 5 was measured for the H2, H3 and H6 protons of $TmDOTP^{5-}$ in both rat and mouse brains, corresponding to an error of less than 0.05 in the pH_e measurement, according to our previous SNR-based estimations [50]. Using these two results, we estimate that the error in ΔpH measurement is less than 0.15.

A limitation of our study is the difference in resolution between pH_i and pH_e maps. While pH_i with AACID allows measurements at high resolution (0.76mm×0.76mm×1.00mm in rats, 0.6mm×0.6mm×1.00mm in mice), the use of an MRSI-based sequence limits the pH_e

resolution to 1mm isotropic. Thus, to obtain the ΔpH images, we resampled the pH_e images to the resolution of the pH_i images using a spatially weighted contribution approach (Fig. 1L). In the future, pH_e imaging at sub-millimeter resolution could be achieved by using a special k-space sampling strategy, called REduced Spherical Encoding with GAussian Weighting (RESEGAW), which was previously demonstrated in rat brain [43]. Another limitation of this study is the relatively low number of animals used for each tumor type (n=2 for RG2 and U87, n=3 for GL261). The goal of this paper was to demonstrate the feasibility of imaging the transmembrane pH gradient in two different species (rats and mice) with various types of gliomas (RG2, U87 and GL261). However, the relatively low number of animals per group does not allow a more detailed statistical analysis and comparison between different tumor types. In the future, increasing the number of animals for each tumor type will allow a more thorough comparative analysis between different types of gliomas, including assessing reproducibility. A potential limitation for clinical translation of ΔpH imaging is the use of $TmDOTP^{5-}$ (or other similar Ln^{3+}-based BIRDS agents), which are not FDA-approved. In the current work $TmDOTP^{5-}$ was used as proof of concept, demonstrating feasibility of ΔpH imaging in preclinical settings. We are currently developing pH_e sensors for BIRDS based on divalent transition metal ions (e.g., Fe^{2+}, Ni^{2+}, or Co^{2+})[78], which could be ideal candidates for clinical translation.

In conclusion, our study successfully demonstrated the feasibility of obtaining transmembrane pH gradient images at sub-millimeter resolution in both rat and mouse brains with various types of gliomas. We successfully obtained for the first time pH_e imaging with BIRDS at 1mm isotropic resolution in mouse brains. The ability to image the transmembrane pH gradient in rodents opens new avenues for better understanding the resistance mechanisms in brain cancer. ΔpH imaging could be used to investigate the effects of drugs targeting the transmembrane pH difference which represents a potential therapeutic target [14–16]. For example, inhibition of proton-coupled transmembrane monocarboxylate transporters MCT1 or MCT4[79] represents a promising therapeutic target for glioblastoma [5, 80–84], because this type of brain tumor is highly glycolytic and strongly dependent on proton (H^+)/lactate transporters[6]. Moreover, ΔpH imaging might help us understand how manipulation of pH_e and/or pH_i could regulate drug entry into cells [17–21]. Ultimately, this imaging technique may play a pivotal role in development of improved and personalized therapies not only for brain cancers, but also for treatment of other types of cancers.

Supplementary Material

Refer to Web version on PubMed Central for supplementary material.

ACKNOWLEDGMENTS

We thank Monique Thomas, Peter Brown, Robin DeGraaf, Terry Nixon, Scott McIntyre, Peter Herman, and the rest of the staff at the Yale MRRC for technical support and for assistance with animal care. We thank DeFeyter's group at Yale University for providing the GL261 tumor cells. This study was supported by the NIH grants R21-NS132543, R01-CA280871, R01-EB023366.

DATA AVAILABILITY STATEMENT

The data that support the findings of this study are available from the corresponding author upon reasonable request.

Abbreviations:

AACID	Amine and Amide Concentration-Independent Detection
BIRDS	Biosensor Imaging of Redundant Deviation in Shifts
CEST	Chemical Exchange Saturation Transfer
$DOTP^{5-}$	1,4,7,10-tetraazacyclododecane-1,4,7,10-tetrakis(methylenephosphonate)
DMEM	Dulbecco's modified eagle's medium
EPI	Echo-Planar Imaging
FOV	field-of-view
Ln^{3+}	lanthanide ion
MCT	monocarboxylic acid transporter
MRSI	Magnetic Resonance Spectroscopic Imaging
PET	Positron Emission Tomography
pH_e	extracellular pH
pH_i	intracellular pH
RESEGAW	REduced Spherical Encoding with GAussian Weighting
RF	radio frequency
ROI	region of interest
SLR	Shinnar-Le Roux
ΔpH	transmembrane pH gradient
Tm^{3+}	thulium ion
WASSR	WAter Saturation Shift Referencing

REFERENCES

1. Gatenby RA and Gillies RJ, Why do cancers have high aerobic glycolysis? Nat Rev Cancer, 2004. 4(11): p. 891–9. [PubMed: 15516961]
2. Warburg O, On respiratory impairment in cancer cells. Science, 1956. 124(3215): p. 269–70. [PubMed: 13351639]

3. Webb BA, et al. , Dysregulated pH: a perfect storm for cancer progression. Nat Rev Cancer, 2011. 11(9): p. 671–7. [PubMed: 21833026]
4. Hyder F and Khan MH, Dysregulated proton and sodium gradients highlight cancer invasion and proliferation. Transl Oncol, 2022. 16: p. 101310. [PubMed: 34896853]
5. Park SJ, et al. , An overview of MCT1 and MCT4 in GBM: small molecule transporters with large implications. Am J Cancer Res, 2018. 8(10): p. 1967–1976. [PubMed: 30416849]
6. Harguindey S, et al. , Hydrogen Ion Dynamics of Cancer and a New Molecular, Biochemical and Metabolic Approach to the Etiopathogenesis and Treatment of Brain Malignancies. Int J Mol Sci, 2019. 20(17).
7. Ross BD, et al. , 31P NMR spectroscopy of the in vivo metabolism of an intracerebral glioma in the rat. Magn Reson Med, 1988. 6(4): p. 403–17. [PubMed: 3380002]
8. Ross BD, et al. , In vivo 31P and 2H NMR [corrected] studies of rat brain tumor pH and blood flow during acute hyperglycemia: differential effects between subcutaneous and intracerebral locations. Magn Reson Med, 1989. 12(2): p. 219–34. [PubMed: 2559287]
9. Gerweck LE and Seetharaman K, Cellular pH gradient in tumor versus normal tissue: potential exploitation for the treatment of cancer. Cancer Res, 1996. 56(6): p. 1194–8. [PubMed: 8640796]
10. Gerweck LE, The pH difference between tumor and normal tissue offers a tumor specific target for the treatment of cancer. Drug Resist Updat, 2000. 3(1): p. 49–50. [PubMed: 11498365]
11. Stubbs M, et al. , An assessment of 31P MRS as a method of measuring pH in rat tumours. NMR Biomed, 1992. 5(6): p. 351–9. [PubMed: 1489671]
12. Stubbs M, et al. , Metabolic consequences of a reversed pH gradient in rat tumors. Cancer Res, 1994. 54(15): p. 4011–6. [PubMed: 8033132]
13. Hashim AI, et al. , Imaging pH and metastasis. NMR Biomed, 2011. 24(6): p. 582–91. [PubMed: 21387439]
14. Gerweck LE, Tumor pH: implications for treatment and novel drug design. Semin Radiat Oncol, 1998. 8(3): p. 176–82. [PubMed: 9634494]
15. Kozin SV, Shkarin P, and Gerweck LE, The cell transmembrane pH gradient in tumors enhances cytotoxicity of specific weak acid chemotherapeutics. Cancer Res, 2001. 61(12): p. 4740–3. [PubMed: 11406545]
16. Evelhoch JL, pH and therapy of human cancers. Novartis Found Symp, 2001. 240: p. 68–80; discussion 80–4, 152–3. [PubMed: 11727937]
17. Altan N, et al. , Defective acidification in human breast tumor cells and implications for chemotherapy. J Exp Med, 1998. 187(10): p. 1583–98. [PubMed: 9584137]
18. Larsen AK, Escargueil AE, and Skladanowski A, Resistance mechanisms associated with altered intracellular distribution of anticancer agents. Pharmacol Ther, 2000. 85(3): p. 217–29. [PubMed: 10739876]
19. Raghunand N, et al. , Enhancement of chemotherapy by manipulation of tumour pH. Br J Cancer, 1999. 80(7): p. 1005–11. [PubMed: 10362108]
20. Raghunand N, Mahoney BP, and Gillies RJ, Tumor acidity, ion trapping and chemotherapeutics. II. pH-dependent partition coefficients predict importance of ion trapping on pharmacokinetics of weakly basic chemotherapeutic agents. Biochem Pharmacol, 2003. 66(7): p. 1219–29. [PubMed: 14505801]
21. Raghunand N, et al. , pH and drug resistance. II. Turnover of acidic vesicles and resistance to weakly basic chemotherapeutic drugs. Biochem Pharmacol, 1999. 57(9): p. 1047–58. [PubMed: 10796075]
22. Coman D, et al. , Imaging the intratumoral-peritumoral extracellular pH gradient of gliomas. NMR Biomed, 2016. 29(3): p. 309–19. [PubMed: 26752688]
23. Gillies RJ, Liu Z, and Bhujwalla Z, 31P-MRS measurements of extracellular pH of tumors using 3-aminopropylphosphonate. Am J Physiol, 1994. 267(1 Pt 1): p. C195–203. [PubMed: 8048479]
24. Petroff OA, et al. , In vivo phosphorus nuclear magnetic resonance spectroscopy in status epilepticus. Ann Neurol, 1984. 16(2): p. 169–77. [PubMed: 6476792]
25. He S, et al. , Development of novel 19F NMR pH indicators: synthesis and evaluation of a series of fluorinated vitamin B6 analogues. Bioorg Med Chem, 1998. 6(9): p. 1631–9. [PubMed: 9801834]

26. Mason RP, Transmembrane pH gradients in vivo: measurements using fluorinated vitamin B6 derivatives. Curr Med Chem, 1999. 6(6): p. 481–99. [PubMed: 10213795]
27. Ojugo AS, et al. , Measurement of the extracellular pH of solid tumours in mice by magnetic resonance spectroscopy: a comparison of exogenous (19)F and (31)P probes. NMR Biomed, 1999. 12(8): p. 495–504. [PubMed: 10668042]
28. Drake LR, Hillmer AT, and Cai Z, Approaches to PET Imaging of Glioblastoma. Molecules, 2020. 25(3).
29. Frullano L, et al. , Bimodal MR-PET agent for quantitative pH imaging. Angew Chem Int Ed Engl, 2010. 49(13): p. 2382–4. [PubMed: 20191650]
30. Pollard AC, et al. , Radiometal-Based PET/MRI Contrast Agents for Sensing Tumor Extracellular pH. Biosensors, 2022. 12(2): p. 134. [PubMed: 35200394]
31. Ward KM and Balaban RS, Determination of pH using water protons and chemical exchange dependent saturation transfer (CEST). Magn Reson Med, 2000. 44(5): p. 799–802. [PubMed: 11064415]
32. Ward KM, Aletras AH, and Balaban RS, A new class of contrast agents for MRI based on proton chemical exchange dependent saturation transfer (CEST). J Magn Reson, 2000. 143(1): p. 79–87. [PubMed: 10698648]
33. Kim J, et al. , A review of optimization and quantification techniques for chemical exchange saturation transfer MRI toward sensitive in vivo imaging. Contrast Media Mol Imaging, 2015. 10(3): p. 163–178. [PubMed: 25641791]
34. McVicar N, et al. , Quantitative tissue pH measurement during cerebral ischemia using amine and amide concentration-independent detection (AACID) with MRI. J Cereb Blood Flow Metab, 2014. 34(4): p. 690–8. [PubMed: 24496171]
35. Kim M, et al. , Water saturation shift referencing (WASSR) for chemical exchange saturation transfer (CEST) experiments. Magn Reson Med, 2009. 61(6): p. 1441–50. [PubMed: 19358232]
36. Longo DL, et al. , In Vivo Imaging of Tumor Metabolism and Acidosis by Combining PET and MRI-CEST pH Imaging. Cancer Res, 2016. 76(22): p. 6463–6470. [PubMed: 27651313]
37. Jones KM, et al. , Clinical Translation of Tumor Acidosis Measurements with AcidoCEST MRI. Mol Imaging Biol, 2017. 19(4): p. 617–625. [PubMed: 27896628]
38. Lindeman LR, et al. , A comparison of exogenous and endogenous CEST MRI methods for evaluating in vivo pH. Magn Reson Med, 2018. 79(5): p. 2766–2772. [PubMed: 29024066]
39. Chen LQ, et al. , Evaluations of extracellular pH within in vivo tumors using acidoCEST MRI. Magn Reson Med, 2014. 72(5): p. 1408–17. [PubMed: 24281951]
40. Coman D, et al. , Brain temperature and pH measured by (1)H chemical shift imaging of a thulium agent. NMR Biomed, 2009. 22(2): p. 229–39. [PubMed: 19130468]
41. Coman D, Trubel HK, and Hyder F, Brain temperature by Biosensor Imaging of Redundant Deviation in Shifts (BIRDS): comparison between TmDOTP5- and TmDOTMA. NMR Biomed, 2010. 23(3): p. 277–85. [PubMed: 19957287]
42. Coman D, et al. , A lanthanide complex with dual biosensing properties: CEST (chemical exchange saturation transfer) and BIRDS (biosensor imaging of redundant deviation in shifts) with europium DOTA-tetraglycinate. NMR Biomed, 2011. 24(10): p. 1216–25. [PubMed: 22020775]
43. Coman D, et al. , In vivo three-dimensional molecular imaging with Biosensor Imaging of Redundant Deviation in Shifts (BIRDS) at high spatiotemporal resolution. NMR Biomed, 2013. 26(11): p. 1589–95. [PubMed: 23881869]
44. Maritim S, et al. , Mapping Extracellular pH of Gliomas in Presence of Superparamagnetic Nanoparticles: Towards Imaging the Distribution of Drug-Containing Nanoparticles and Their Curative Effect on the Tumor Microenvironment. Contrast Media Mol Imaging, 2017. 2017: p. 3849373. [PubMed: 29362558]
45. Rao JU, et al. , Temozolomide arrests glioma growth and normalizes intratumoral extracellular pH. Sci Rep, 2017. 7(1): p. 7865. [PubMed: 28801587]
46. Huang Y, et al. , Towards longitudinal mapping of extracellular pH in gliomas. NMR Biomed, 2016. 29(10): p. 1364–72. [PubMed: 27472471]

47. Mihailovic JM, et al. , High-resolution pH imaging using ratiometric chemical exchange saturation transfer combined with biosensor imaging of redundant deviation in shifts featuring paramagnetic DOTA-tetraglycinate agents. NMR Biomed, 2022. 35(5): p. e4658. [PubMed: 34837412]
48. Borde T, et al. , Idarubicin-Loaded ONCOZENE Drug-Eluting Bead Chemoembolization in a Rabbit Liver Tumor Model: Investigating Safety, Therapeutic Efficacy, and Effects on Tumor Microenvironment. J Vasc Interv Radiol, 2020.
49. Savic LJ, et al. , Molecular MRI of the Immuno-Metabolic Interplay in a Rabbit Liver Tumor Model: A Biomarker for Resistance Mechanisms in Tumor-targeted Therapy? Radiology, 2020. 296(3): p. 575–583. [PubMed: 32633675]
50. Coman D, et al. , Extracellular pH mapping of liver cancer on a clinical 3T MRI scanner. Magn Reson Med, 2020. 83(5): p. 1553–1564. [PubMed: 31691371]
51. Savic LJ, et al. , Molecular Imaging of Extracellular Tumor pH to Reveal Effects of Locoregional Therapy on Liver Cancer Microenvironment. Clin Cancer Res, 2020. 26(2): p. 428–438. [PubMed: 31582517]
52. Doemel LA, et al. , Comparison of metabolic and immunologic responses to transarterial chemoembolization with different chemoembolic regimens in a rabbit VX2 liver tumor model. Eur Radiol, 2022. 32(4): p. 2437–2447. [PubMed: 34718844]
53. Krex D, et al. , Long-term survival with glioblastoma multiforme. Brain, 2007. 130(Pt 10): p. 2596–606. [PubMed: 17785346]
54. Miller KD, et al. , Brain and other central nervous system tumor statistics, 2021. CA Cancer J Clin, 2021. 71(5): p. 381–406. [PubMed: 34427324]
55. Ostrom QT, Gittleman H, and Stetson L, Barnholtz-Sloan JS,(2015). Epidemiology of gliomas. Cancer Treatment and Research. 163: p. 1–14. [PubMed: 25468222]
56. Pearson JRD and Regad T, Targeting cellular pathways in glioblastoma multiforme. Signal Transduct Target Ther, 2017. 2: p. 17040. [PubMed: 29263927]
57. Wechsler W, et al. , Pathology of experimental neurogenic tumors chemically induced during prenatal and postnatal life. Annals of the New York Academy of Sciences, 1969. 159(2): p. 360–408.
58. Pontén J and Macintyre EH, Long term culture of normal and neoplastic human glia. Acta Pathol Microbiol Scand, 1968. 74(4): p. 465–86. [PubMed: 4313504]
59. Ausman JI, Shapiro WR, and Rall DP, Studies on the chemotherapy of experimental brain tumors: development of an experimental model. Cancer Res, 1970. 30(9): p. 2394–400. [PubMed: 5475483]
60. Hedaya MA, Elmquist WF, and Sawchuk RJ, Probenecid inhibits the metabolic and renal clearances of zidovudine (AZT) in human volunteers. Pharm Res, 1990. 7(4): p. 411–7. [PubMed: 2362917]
61. Robbins N, et al. , The history and future of probenecid. Cardiovasc Toxicol, 2012. 12(1): p. 1–9. [PubMed: 21938493]
62. Masereeuw R, et al. , Probenecid interferes with renal oxidative metabolism: a potential pitfall in its use as an inhibitor of drug transport. Br J Pharmacol, 2000. 131(1): p. 57–62. [PubMed: 10960069]
63. Hyder F and Coman D, Imaging Extracellular Acidification and Immune Activation in Cancer. Curr Opin Biomed Eng, 2021. 18: p. 100278. [PubMed: 33997581]
64. Savic LJ, et al. , A high-throughput imaging platform to characterize extracellular pH in organotypic three-dimensional in vitro models of liver cancer. NMR Biomed, 2021. 34(3): p. e4465. [PubMed: 33354836]
65. Qi Q, et al. , Glucose Infusion Induced Change in Intracellular pH and Its Relationship with Tumor Glycolysis in a C6 Rat Model of Glioblastoma. Mol Imaging Biol, 2023. 25(2): p. 271–282. [PubMed: 36418769]
66. Walsh JJ, et al. , Imaging Hallmarks of the Tumor Microenvironment in Glioblastoma Progression. Front Oncol, 2021. 11: p. 692650. [PubMed: 34513675]
67. Warburg O, On the origin of cancer cells. Science, 1956. 123(3191): p. 309–14. [PubMed: 13298683]

68. Mahoney BP, et al. , Tumor acidity, ion trapping and chemotherapeutics. I. Acid pH affects the distribution of chemotherapeutic agents in vitro. Biochem Pharmacol, 2003. 66(7): p. 1207–18. [PubMed: 14505800]
69. Lim H, et al. , Longitudinal Measurements of Intra- and Extracellular pH Gradient in a Rat Model of Glioma. Tomography, 2018. 4(2): p. 46–54. [PubMed: 30206544]
70. Srivastava J, Barber DL, and Jacobson MP, Intracellular pH sensors: design principles and functional significance. Physiology (Bethesda), 2007. 22: p. 30–9. [PubMed: 17289928]
71. Pouysségur J, et al. , Cytoplasmic pH, a key determinant of growth factor-induced DNA synthesis in quiescent fibroblasts. FEBS Lett, 1985. 190(1): p. 115–9. [PubMed: 4043390]
72. Moolenaar WH, Effects of growth factors on intracellular pH regulation. Annu Rev Physiol, 1986. 48: p. 363–76. [PubMed: 3010817]
73. Kapus A, et al. , A pH-sensitive and voltage-dependent proton conductance in the plasma membrane of macrophages. J Gen Physiol, 1993. 102(4): p. 729–60. [PubMed: 8270911]
74. Denker SP, et al. , Direct binding of the Na--H exchanger NHE1 to ERM proteins regulates the cortical cytoskeleton and cell shape independently of H(+) translocation. Mol Cell, 2000. 6(6): p. 1425–36. [PubMed: 11163215]
75. Lagadic-Gossmann D, Huc L, and Lecureur V, Alterations of intracellular pH homeostasis in apoptosis: origins and roles. Cell Death Differ, 2004. 11(9): p. 953–61. [PubMed: 15195071]
76. Matsuyama S, et al. , Changes in intramitochondrial and cytosolic pH: early events that modulate caspase activation during apoptosis. Nat Cell Biol, 2000. 2(6): p. 318–25. [PubMed: 10854321]
77. Hanahan D and Weinberg RA, Hallmarks of cancer: the next generation. Cell, 2011. 144(5): p. 646–74. [PubMed: 21376230]
78. Olatunde AO, et al. , Six, Seven or Eight Coordinate Fe(II), Co(II) or Ni(II) Complexes of Amide-Appended Tetraazamacrocycles for ParaCEST Thermometry. Chemistry, 2015. 21(50): p. 18290–300. [PubMed: 26494320]
79. Halestrap AP, The SLC16 gene family - structure, role and regulation in health and disease. Mol Aspects Med, 2013. 34(2–3): p. 337–49. [PubMed: 23506875]
80. Miranda-Gonçalves V, et al. , Monocarboxylate transporters (MCTs) in gliomas: expression and exploitation as therapeutic targets. Neuro Oncol, 2013. 15(2): p. 172–88. [PubMed: 23258846]
81. Lim KS, et al. , Inhibition of monocarboxylate transporter-4 depletes stem-like glioblastoma cells and inhibits HIF transcriptional response in a lactate-independent manner. Oncogene, 2014. 33(35): p. 4433–41. [PubMed: 24077291]
82. Morrot A, et al. , Metabolic Symbiosis and Immunomodulation: How Tumor Cell-Derived Lactate May Disturb Innate and Adaptive Immune Responses. Front Oncol, 2018. 8: p. 81. [PubMed: 29629338]
83. Kennedy KM and Dewhirst MW, Tumor metabolism of lactate: the influence and therapeutic potential for MCT and CD147 regulation. Future Oncol, 2010. 6(1): p. 127–48. [PubMed: 20021214]
84. Pérez-Escuredo J, et al. , Monocarboxylate transporters in the brain and in cancer. Biochim Biophys Acta, 2016. 1863(10): p. 2481–97. [PubMed: 26993058]

Significance:

Imaging the transmembrane pH gradient could provide a powerful clinical tool for assessing aggressiveness of tumor cells, understanding tumor responsiveness, monitoring treatment efficacy, or guiding localized drug delivery, to improve personalized cancer treatment.

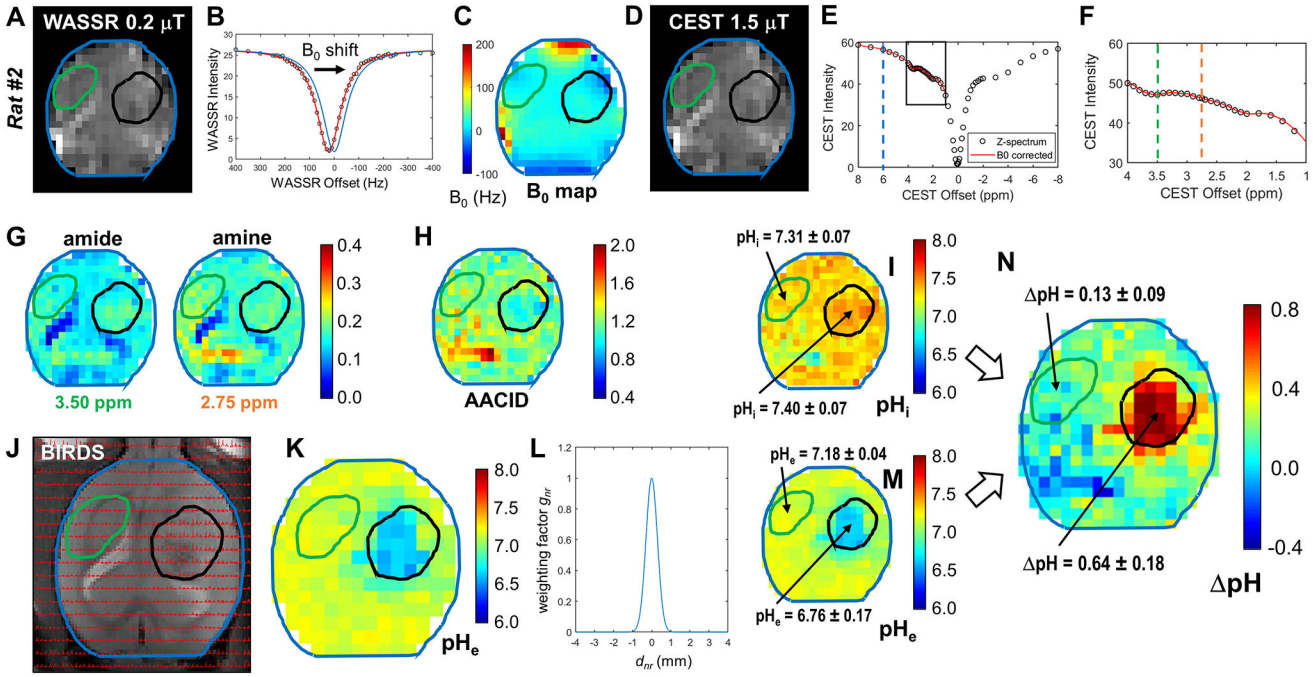

Fig.1. High resolution transmembrane pH gradient (ΔpH) imaging in rat brain with RG2 tumor.

The pH_i mapping is based on AACID method and is described in **A-I**. **(A)** EPI-based images for WASSR were obtained at various saturation frequency offsets in the range from −500 to 500 Hz using a B_1 field of 0.2uT. The blue and black boundaries represent the brain and tumor, respectively, as obtained by T_1-weighted MRI. **(B)** A least-squares fit with a Lorentzian function (red line) was used to calculate the B_0 shift in each voxel, where the blue line (centered at 0Hz) indicates the B_0 shifted Lorentzian fit. **(C)** B_0 map generated using the B_0 shifts measured in each voxel. **(D)** EPI-based images for AACID were obtained at various saturation frequency offsets in the range from −8000 to 8000 ppm using a B_1 field of 1.5uT. **(E)** A Z-spectrum was generated in each voxel from the EPI images. The "B_0 corrected" Z-spectrum (red line) was obtained using a spline interpolation at 1Hz resolution followed by a B_0 field correction using the B_0 shift measured with WASSR. **(F)** The inset indicated by the black box in **E**. **(G)** Amide and amine intensity maps were obtained from the "B_0 corrected" Z-spectrum using the amide signal at 3.5ppm (green dashed line in **F**) and amine signal at 2.75ppm (orange dashed line in **F**). **(H)** The AACID ratio map was calculated from the amide and amine intensities and using as reference the signal at 6.0ppm (blue dashed line in **E**) according to eq.1. **(I)** The pH_i map was calculated from the AACID ratio according to eq.2. The average pH_i values measured in the tumor and normal tissue were 7.40 ± 0.07 and 7.31 ± 0.07, respectively. The pH_e mapping is based on BIRDS method and is described in **J-M**. **(J)** A T_1-weighted MRI was used to localize and define an ROI for the tumor (black contour) and delineate the entire brain (blue contour). A second ROI corresponding to normal brain tissue (green contour) was defined in the contralateral hemisphere for comparisons with tumor measurements. The MRSI spectra from BIRDS in each voxel are shown in red, overlayed on the anatomical image. **(K)** The native pH_e map at 1mm isotropic resolution was calculated from the chemical shifts of H2, H3 and H6 $TmDOTP^{5-}$ protons according to eq.3. **(L)** Gaussian weighting factor g_{nr} as function of

distance d_{nr} between voxel n from the native pH_e map and voxel r from the resampled pH_e map calculated according to eq.4 with b=0.3 mm. **(M)** The resampled pH_e map was obtained from the native pH_e map as a spatially weighted contribution using the Gaussian weighting factor g_{nr} according to eq.5. The resampled pH_e map (**M**) shows similar features as the native pH_e map (**K**). The average pH_e values measured using the resampled pH_e map in the tumor and normal tissue were 6.76 ± 0.17 and 7.18 ± 0.04, respectively. **(N)** Transmembrane pH gradient calculated as $\Delta pH=pH_i-pH_e$, where the pH_e values are from the resampled pH_e map. The average ΔpH values in the tumor and normal tissue ROIs were 0.64 ± 0.18 and 0.13 ± 0.09, respectively. The average pH_i, pH_e and ΔpH values for all animals investigated are given in Table 1.

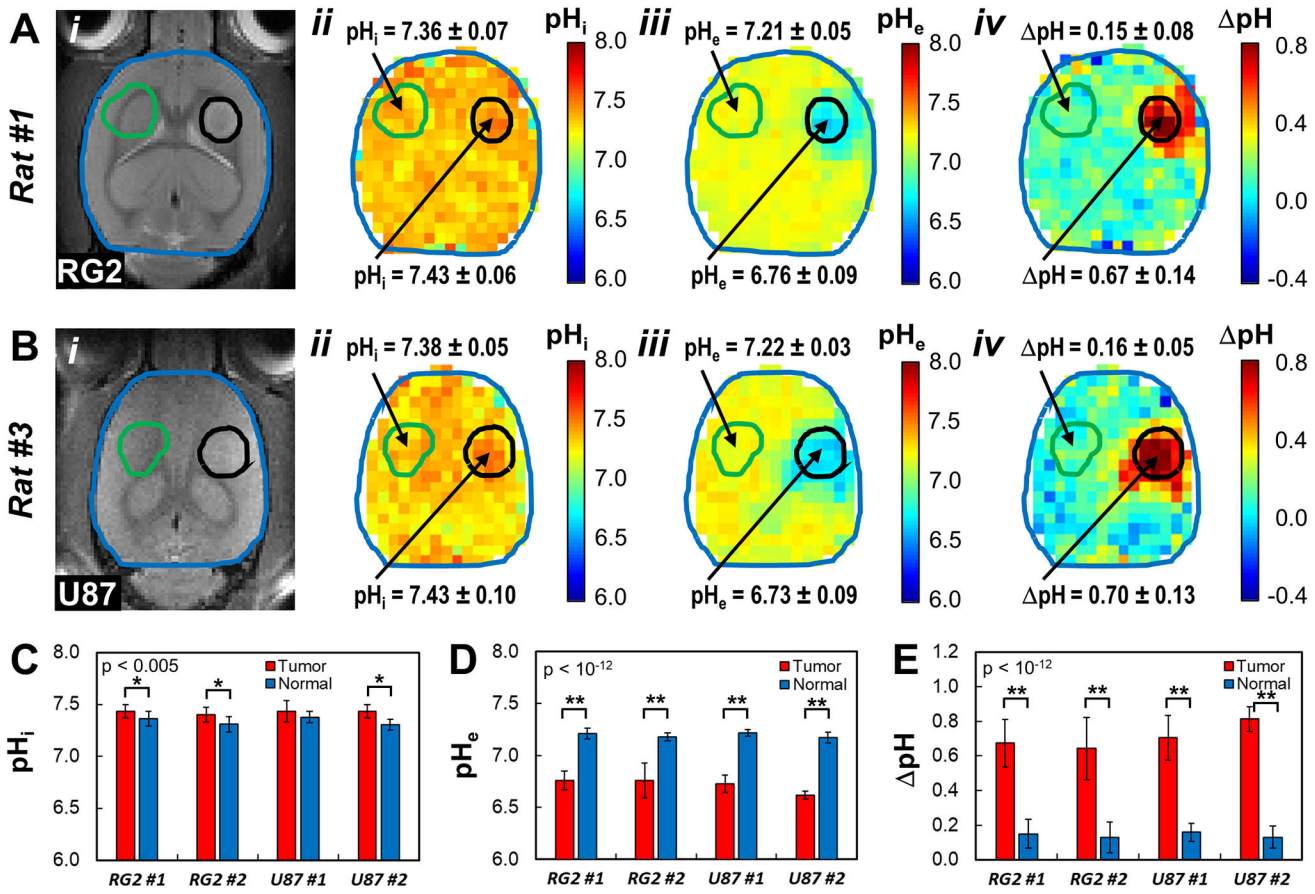

Fig.2. Examples of transmembrane pH gradient imaging in rat brains with RG2 and U87 tumors.

Measurements from rat brains with RG2 tumors are shown in the top row **(A, *i-iv*)**, while those from U87 tumors in the middle row **(B, *i-iv*)**. The T_1-weighted MR images (**A*i* and B*i***) were used to localize and define the ROI for the tumor (black contour) and delineate the entire brain (blue contour). A second ROI corresponding to normal brain tissue (green contour) was defined in the contralateral hemisphere for comparisons with tumor measurements. The pH_i maps (**A*ii* and B*ii***) indicate slightly higher pH_i values inside both RG2 and U87 tumors compared to normal brain tissue. The pH_e maps (**A*iii* and B*iii***) show significantly lower pH_e values inside both RG2 and U87 tumors compared to normal brain tissue. As a result, the transmembrane pH gradient ΔpH (**A*iv* and B*iv***) was significantly higher inside both RG2 and U87 tumors compared to normal brain tissue. For easy comparison, the average measurements for all animals investigated are shown as histograms for pH_i **(C)**, pH_e **(D)** and ΔpH **(E)** in both tumor (red) and normal (blue) regions. The error bars in each histogram indicate the standard deviation. Except U87#1, the average pH_i values (**C**) were significantly larger in tumors compared to normal tissue (*, $p<0.005$). For all animals, the average pH_e (**D**) and ΔpH (**E**) values were significantly different (**, $p<10^{-12}$) when comparing tumors with normal tissue. The numerical pH_i, pH_e and ΔpH values for all animals are given in Table 1.

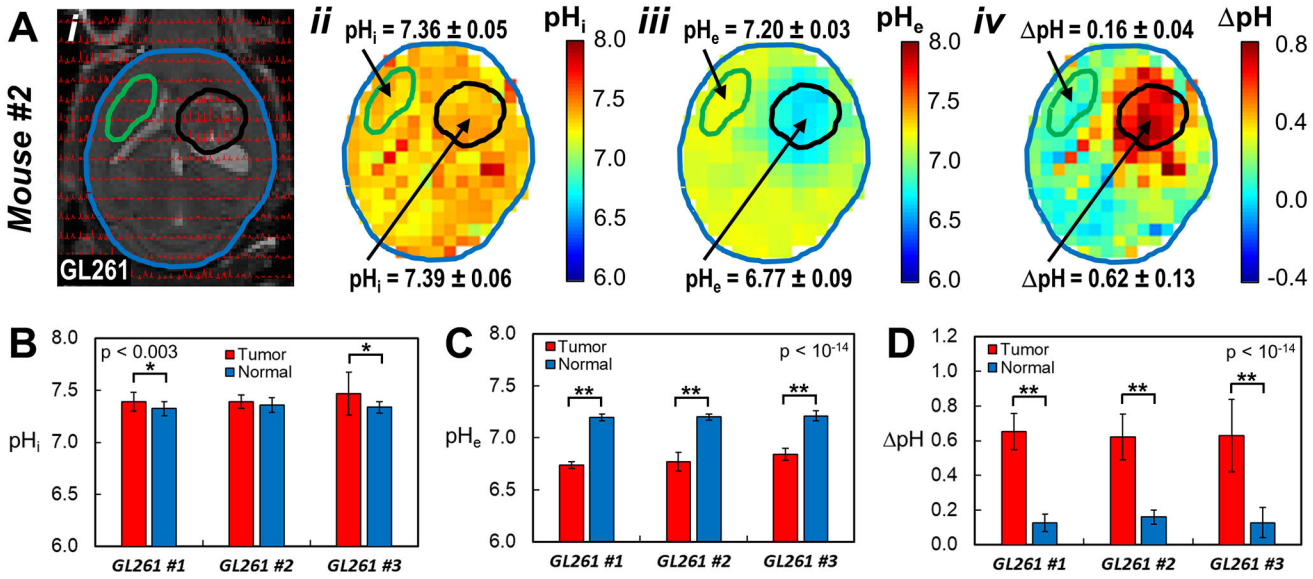

Fig.3. Transmembrane pH gradient imaging in mouse brains with GL261 tumors.

The T_1-weighted MRI **(A*i*)** was used to localize and define the ROI for the tumor (black contour) and delineate the entire brain (blue contour). A second ROI corresponding to normal brain tissue (green contour) was defined in the contralateral hemisphere for comparisons with tumor measurements. The pH_i map using AACID **(A*ii*)** shows only a slightly higher pH_i value inside the GL261 tumor compared to normal brain tissue. The pH_e map using BIRDS **(A*iii*)** shows a significantly lower pH_e value inside the tumor compared to normal brain tissue. Thus, the transmembrane pH gradient ΔpH **(A*iv*)** was significantly higher inside the GL261 tumor compared to normal brain tissue. For easy comparison, the average measurements for all animals investigated are shown as histograms for pH_i **(B)**, pH_e **(C)** and ΔpH **(D)** in both tumor (red) and normal (blue) regions. The error bars in each histogram indicate the standard deviation. For GL261#1 and GL261#3, the average pH_i values (**B**) were significantly larger in tumors compared to normal tissue (*, $p<0.003$). The average pH_e (**D**) and ΔpH (**E**) values were significantly different (**, $p<10^{-14}$) in all animals when comparing tumors with normal tissue. The numerical pH_i, pH_e and ΔpH values for all animals investigated are given in Table 1.

Table 1.

The average and the standard deviation values for pH_i, pH_e and ΔpH in tumor and normal brain tissue in rat and mouse brains implanted with various tumor cell lines. The number of voxels and the volume of the ROI investigated for both tumor and normal brain tissue is also indicated. In some cases, the ROI volume of normal brain tissue was different than that of the tumor to avoid inclusion of cerebrospinal fluid areas in the average pH estimation.

Animal ID	Tumor cell line	Tumor					Normal				
		pH_i	pH_e	ΔpH	Number of voxels	ROI volume (μL)	pH_i	pH_e	ΔpH	Number of voxels	ROI volume (μL)
Rat #1	RG2	7.43 ± 0.06	6.76 ± 0.09	0.67 ± 0.14	14	8.1	7.36 ± 0.07	7.21 ± 0.05	0.15 ± 0.08	18	10.4
Rat #2	RG2	7.40 ± 0.07	6.76 ± 0.17	0.64 ± 0.18	37	21.5	7.31 ± 0.07	7.18 ± 0.04	0.13 ± 0.09	27	15.7
Rat #3	U87	7.43 ± 0.10	6.73 ± 0.09	0.70 ± 0.13	14	8.1	7.38 ± 0.05	7.22 ± 0.03	0.16 ± 0.05	13	7.5
Rat #4	U87	7.43 ± 0.07	6.62 ± 0.04	0.81 ± 0.07	11	6.4	7.30 ± 0.05	7.17 ± 0.05	0.13 ± 0.06	12	7.0
Mouse #1	GL261	7.39 ± 0.09	6.74 ± 0.03	0.65 ± 0.10	29	10.3	7.32 ± 0.04	7.20 ± 0.03	0.13 ± 0.05	21	7.4
Mouse #2	GL261	7.39 ± 0.06	6.77 ± 0.09	0.62 ± 0.13	26	9.2	7.36 ± 0.05	7.20 ± 0.03	0.16 ± 0.04	14	5.0
Mouse #3	GL261	7.47 ± 0.21	6.84 ± 0.06	0.63 ± 0.21	42	15.0	7.34 ± 0.05	7.21 ± 0.05	0.13 ± 0.09	22	7.8